Received: 18 January 2024 | Revised: 6 March 2024 | Accepted: 28 March 2024

DOI: 10.1002/inf2.12549

RESEARCH ARTICLE

WILEY

Two-electron redox chemistry enables potassium-free copper hexacyanoferrate as high-capacity cathode for aqueous Mg-ion battery

Ying Ling[1] | Bing He[2] | Lijie Han[1] | Wenbin Gong[3] | Chaofeng Chang[4] | Qichong Zhang[1]

[1]Key Laboratory of Multifunctional Nanomaterials and Smart Systems, Suzhou Institute of Nano-Tech and Nano-Bionics, Chinese Academy of Sciences, Suzhou, the People's Republic of China

[2]School of Electrical and Electronic Engineering, Nanyang Technological University, Singapore, Singapore

[3]School of Physics and Energy, Xuzhou University of Technology, Xuzhou, the People's Republic of China

[4]Sustainable Energy Laboratory, Faculty of Materials Science and Chemistry, China University of Geosciences Wuhan, Wuhan, the People's Republic of China

Correspondence
Qichong Zhang, Key Laboratory of Multifunctional Nanomaterials and Smart Systems, Suzhou Institute of Nano-Tech and Nano-Bionics, Chinese Academy of Sciences, Suzhou 215123, the People's Republic of China.
Email: qczhang2016@sinano.ac.cn

Funding information
National Key R&D Program of China, Grant/Award Number: 2022YFA1203304; Natural Science Foundation of Jiangsu Province, Grant/Award Number: BK20220288; Suzhou Institute of Nano-Tech and Nano-Bionics, Chinese Academy of Sciences, Grant/Award Number: E1552102

Abstract

Prussian blue analogs (PBAs) are potential contestants for aqueous Mg-ion batteries (AMIBs) on account of their high discharge voltage and three-dimensional open frameworks. However, the low capacity arising from single reaction site severely restricts PBAs' practical applications in high-energy-density AMIBs. Here, an organic acid co-coordination combined with etching method is reported to fabricate defect-rich potassium-free copper hexacyanoferrate with structural water on carbon nanotube fiber (D-CuHCF@CNTF). Benefiting from the high-valence-state reactive sites, arrayed structure and defect effect, the well-designed D-CuHCF@CNTF exhibits an extraordinary reversible capacity of 146.6 mAh g^{-1} with two-electron reaction, nearly close to its theoretical capacity. It is interesting to unlock the reaction mechanism of the Fe^{2+}/Fe^{3+} and Cu^{+}/Cu^{2+} redox couples via x-ray photoelectron spectroscopy. Furthermore, density functional theory calculations reveal that Fe and Cu in potassium-free D-CuHCF participate in charge transfer during the Mg^{2+} insertion/extraction process. As a proof-of-concept demonstration, a rocking-chair fiber-shaped AMIBs was constructed via coupling with the $NaTi_2(PO_4)_3$/CNTF anode, achieving high energy density and impressive mechanical flexibility. This work provides new possibilities to develop potassium-free PBAs with dual-active sites as high-capacity cathodes for wearable AMIBs.

KEYWORDS

aqueous Mg-ion battery, energy-storage fiber, high capacity, Prussian blue analogs, two-electron reaction

Ying Ling and Bing He contributed equally to this study.

1 | INTRODUCTION

The rapid development of wearable electronics has stimulated the demand for safe and efficient energy-storage technologies.[1–5] Aqueous Mg-ion batteries (AMIBs) have attracted widespread concern owing to their satisfactory security, low cost, fast charging capability, and abundant Mg source.[6–8] The significant progress of cathode materials has brought new insight into AMIBs, including tunnel- and layered-type transition metal oxides,[9–13] polyanionic compounds,[14,15] and Prussian blue analogs (PBAs).[16–19] Among them, PBAs have been regarded as the one of the most promising cathodes due to their high discharge voltage and three-dimensional (3D) open frameworks. However, only existing redox reaction of Fe^{2+}/Fe^{3+} in traditional PBAs results in their low capacity and thereby becomes stumbling blocks on the road to development of high-energy-density AMIBs.[20] Therefore, it is greatly significant and urgent to develop a simple and cost-efficient approach to constructing high-capacity PBA cathodes with multiple electron reactions.[21–23]

The formula for PBAs can be described as $A_xM[R(CN)_6]_y \cdot nH_2O$, in which A stands for alkali metal (e.g., Na and K), M and R delegate traditional metal (e.g., Fe, Mn, Co, Zn, Cu, and Ni).[24] Particularly, Cu-PBAs possess a high theoretical capacity over of 150 mAh g^{-1} in aqueous batteries. However, the actual capacity is only 50% of its theoretical capacity which is mainly attributed to the electrochemical inertness of Cu element in Cu-PBAs.[25,26] Thus, various effective approaches have been adopted to settle the above issues, such as element doping,[27,28] defect engineering,[29–33] structural regulation,[34–37] and electrolyte design.[38–41] Mizuno et al. demonstrated reversible Mg^{2+} intercalation/deintercalation in $K_{0.1}Cu[Fe(CN)_6]_{0.7} \cdot 3.6H_2O$ accompanied with a small amount of Cu and Fe redox reactions, delivering a capacity of 50 mAh g^{-1} at 0.1 A g^{-1}.[42] Therefore, activating the Cu active site is extremely important to improve the capacity of Cu-PBAs. In another aspect, owing to the larger radius of hydrated multivalent ions, more intense Jahn–Teller distortions and electrostatic repulsion are induced when performing electrochemical intercalation behavior, thereby reducing ionic conductivity and electrochemical stability.[43–45] To overcome these puzzles, vacancy cavities in PBAs could provide an effective approach for inserting larger ions, thus stabilizing the crystal structure.[46] In addition, PBAs with some defects and structural waters will be beneficial to forming a hydration shell, which can provide more electrostatic shielding and enhance the stability of the crystal structure.[47–49] Lou et al. reported that Cu-replaced MnHCF as the cathodes for long-life Zn-ion batteries, in which fractional Cu replacement and generated Mn vacancies can suppress the Jahn–Teller distortions of the Mn-N_6 octahedra for a Zn-storage stability.[50] Furthermore, Cui et al. synthesized $K_{0.03}Cu[Fe(CN)_6]_{0.65} \cdot 2.6H_2O$ as the host material for the reversible storage of Al^{3+}, and demonstrated that the shielding effect from hydration shell between crystal water and hydrated Al^{3+} on electrostatic repulsion between Al^{3+} and $K_{0.03}Cu[Fe(CN)_6]_{0.65} \cdot 2.6H_2O$.[51] Based on the above analysis, it is foreseeable that rationally designing the crystal structure of PBAs can achieve the activation of dual active sites, suppression of the Jahn–Teller distortions, and construction of electrostatic shielding, which will be beneficial to fabricate high-capacity and high-stability PBA cathodes for AMIBs.

In this work, defect-rich potassium-free CuHCF nanosheet arrays anchored on the surface of a carbon nanotube fiber (D-CuHCF@CNTF) are fabricated by organic acid co-coordination and subsequent etching process, serving as the cathode for fiber-shaped AMIBs (FAMIBs).[52,53] The freestanding D-CuHCF@CNTF with K-vacancy cavities, Cu defects, and structural water not only provides dual active sites and increases the contact area between host materials and electrolyte, but also accommodates the volume variation during the Mg^{2+} insertion/extraction process, accordingly offering prominent capacity and cycling stability.[54,55] In addition, the K-vacancy cavities afford enough interspace for the insertion of Mg^{2+} in D-CuHCF@CNTF, and the Cu defects and structural water can also suppress the Jahn–Teller distortions of Cu-N_6 octahedra and provide electrostatic shielding, thereby achieving the stable crystal structure. Consequently, the resulting D-CuHCF@CNTF cathode delivers a remarkable capacity of 146.6 mAh g^{-1} at 0.5 A g^{-1}. Matched well with the $NaTi_2(PO_4)_3$@CNTF,[56] a rocking-chair twisted-fiber AMIB is successfully constructed, achieving high energy density and outstanding flexibility.[57,58] This work opens a new door to design high-capacity PBA materials with dual-active sites.

2 | RESULTS AND DISCUSSION

2.1 | Materials synthesis and characterization

The preparation process of CuHCF@CNTF is diagrammatically illustrated in Figure 1A. As shown in Figure S1A,B, CNTF with a diameter of ~100 μm acts as a flexible current collector, and a layer of Cu nanoparticles is plated on the CNTF through electrochemical deposition (Figures S1C and 1D). After subsequent oxidation, CuO nanosheets were obtained (Figures S1E and 1F). Accordingly, the corresponding

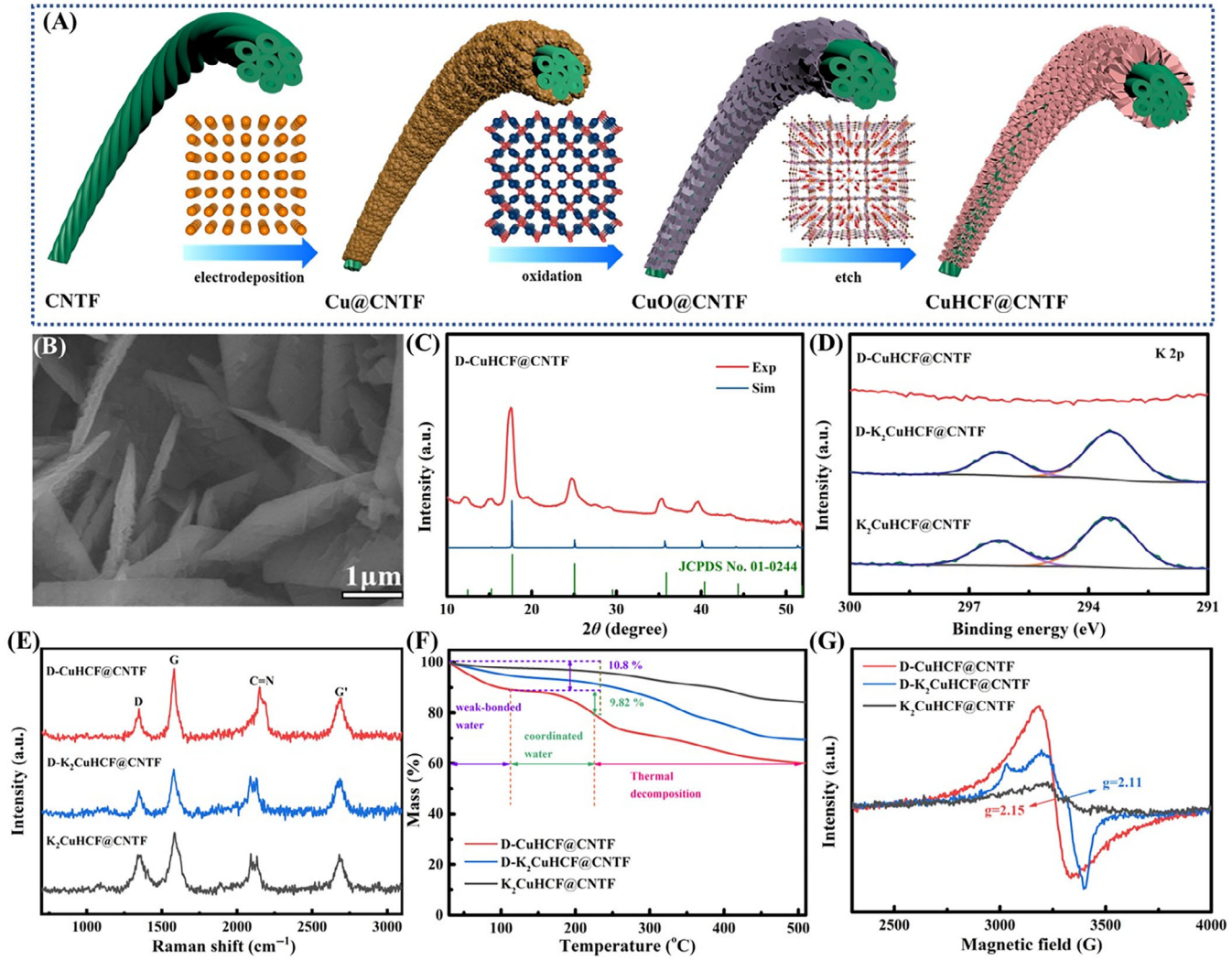

FIGURE 1 Materials synthesis and characterization. (A) The diagram of the synthesis procedure of CuHCF@CNTF. (B) SEM image of D-CuHCF@CNTF. (C) SAXS pattern and computational simulation curve of D-CuHCF@CNTF. (D) XPS spectra of K 2p in D-CuHCF@CNTF, D-K_2CuHCF@CNTF, and K_2CuHCF@CNTF. (E) Raman spectra, (F) TG, and (G) EPR spectra of D-CuHCF@CNTF, D-K_2CuHCF@CNTF, and K_2CuHCF@CNTF.

small-angle x-ray scattering (SAXS) patterns of CNTF, Cu@CNTF, and CuO@CNTF are shown in Figure S2. Finally, three different crystal structures of CuHCF@CNTF (Figure S3) were achieved by the change of ligand introduction method, which was named D-CuHCF@CNTF, D-K_2CuHCF@CNTF, and K_2CuHCF@CNTF. Scanning electron microscopy (SEM) image of D-CuHCF@CNTF in Figure 1B exhibits unique thin nanosheets uniformly grown on the surface of the CNTF, which was obviously different from the other blocky-shaped structures in Figure S4. As the transmission electron microscope (TEM) image in Figure S5, the D-CuHCF@CNTF nanosheets were clearly visible, and the energy dispersive x-ray spectroscopy (EDX) patterns indicate the uniform distribution of the Fe, Cu, C, and N elements. The significant difference in morphology may be attributed to the fact that $K_3[Fe(CN)_6]$ and $C_9H_6O_6$ are co-coordinated with Cu to form nanosheets structure with more K-vacancy cavities, Cu defects, and bound water, which may be favorable for improving the ability of Mg^{2+} insertion. The combined characterization of SAXS and computational simulation of D-CuHCF@CNTF are shown in Figure 1C, in which the D-CuHCF@CNTF highly matched with $Cu_2Fe(CN)_6 \cdot 7H_2O$ (JCPDS No. 01-0244) and the theoretical molecular formulas of D-K_2CuHCF@CNTF and K_2CuHCF@CNTF can be equated as $K_2CuFe(CN)_6$ (Figure S6A). In addition, D-CuHCF@CNTF exhibits superior acid resistance, thus easily eliminating the interference of CuO (Figure S6B). Meanwhile, the x-ray photoelectron spectroscopy (XPS) characterization was measured to verify the difference of D-CuHCF@CNTF,

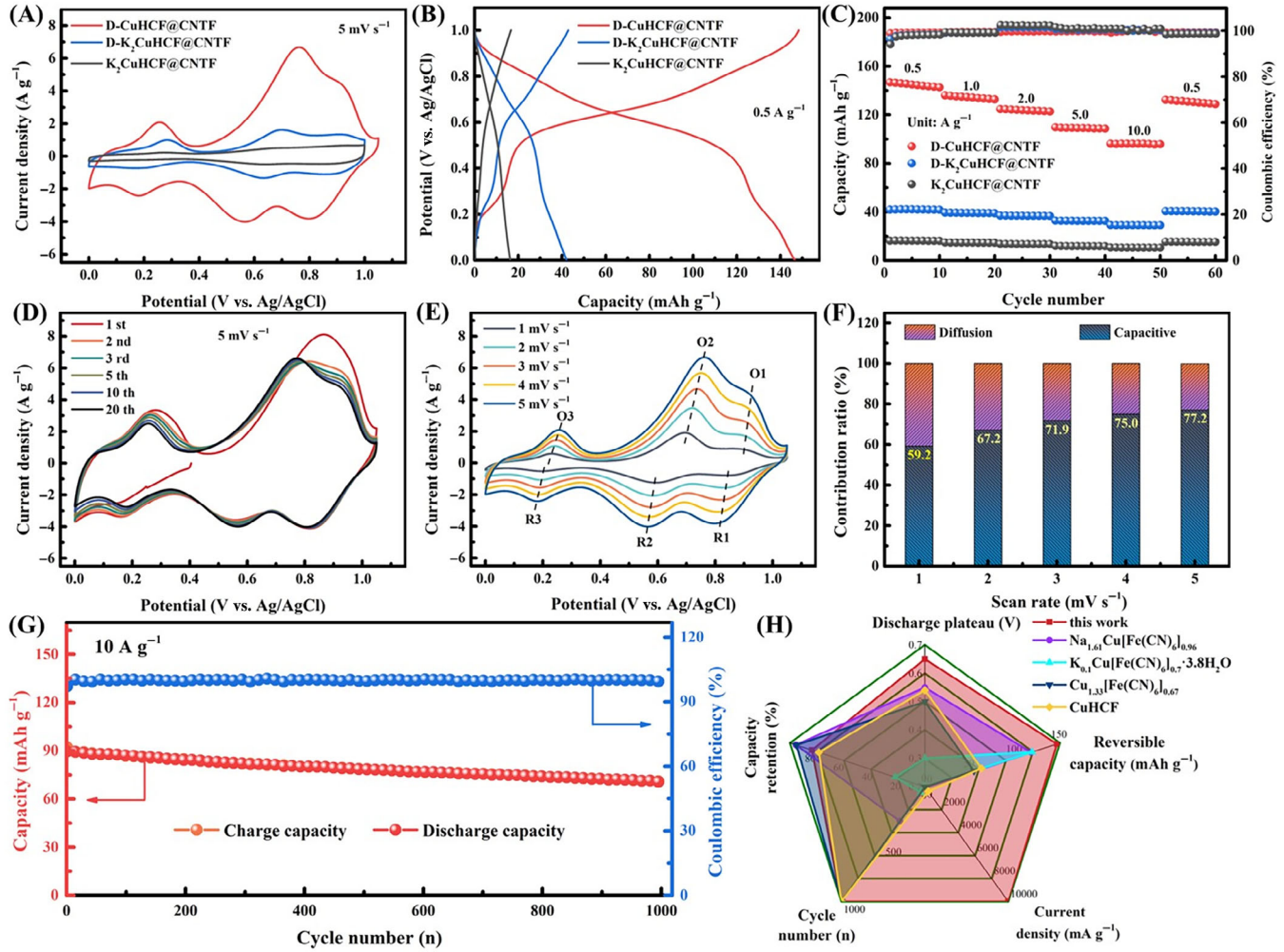

FIGURE 2 Comparison of electrochemical properties. The comparison of (A) CV, (B) GCD curves and (C) rate the performances of D-CuHCF@CNTF, D-K_2CuHCF@CNTF, and K_2CuHCF@CNTF. (D) CV curves of D-CuHCF@CNTF at first 20 cycles at a scan rate of 5 mV s^{-1}. (E) CV curves of D-CuHCF@CNTF at different scan rates. (F) The capacitive contributions of D-CuHCF@CNTF at various scan rates. (G) Cycling performance of D-CuHCF@CNTF at 10 A g^{-1}. (H) Comparison of electrochemical performance between the D-CuHCF and these previously reported PBAs.

D-K_2CuHCF@CNTF, and K_2CuHCF@CNTF on chemical composition, as shown in Figure S7. The high-resolution K 2p XPS spectra of D-K_2CuHCF@CNTF and K_2CuHCF@CNTF (Figure 1D) display two peaks attributed to K^+ (296.28 and 293.48 eV), while the absence in D-CuHCF@CNTF further suggests the existence of K-vacancy cavities, which supply more active sites for Mg^{2+} intercalation. Besides, the Cu 2p and Fe 2p XPS spectra manifest the coresidency of Cu^+ and Cu^{2+}, Fe^{2+} and Fe^{3+}, respectively (Figures S8A,B). Raman spectra were recorded in Figure 1E, a couple of distinct peaks located at 2089 and 2130 cm^{-1} are noticed in D-K_2CuHCF@CNTF and K_2CuHCF@CNTF, which are defined as —C≡N— ligands. In contrast, a visible blue shift is detected in D-CuHCF@CNTF since K-vacancy cavities, Cu defects, and bound water increased the electron cloud intensity. According to the thermogravimetric (TG) analysis (Figure 1F), the mass loss of D-CuHCF@CNTF changes rapidly. It could be attributed to the presence of bound water, containing weakly-bonded water (10.8%) and coordinated water (9.82%), corresponding to about 5.3 H_2O per D-CuHCF@CNTF unit, which is also consistent with the O 1s XPS result in D-CuHCF@CNTF (Figure S9). More importantly, the bound water forms a hydration shell to reduce the electrostatic repulsion between Mg^{2+} and D-CuHCF@CNTF, ensuring the crystal structure stability. To further gain insight in the concentration of Cu defects, the electron paramagnetic resonance (EPR) spectra were carried out (Figure 1G). Compared with D-K_2CuHCF@CNTF and K_2CuHCF@CNTF, D-CuHCF@CNTF displays much higher EPR signal intensity and a slight difference in g value due to the different coordination. Moreover, transition metal vacancies have been reported to give rise to

charge redistribution and mitigate structural deformation, thereby restraining the Jahn–Teller distortions of D-CuHCF@CNTF.

2.2 | Comparison of electrochemical properties

The Mg-storage performance of D-CuHCF@CNTF, D-K_2CuHCF@CNTF, and K_2CuHCF@CNTF was evaluated by a three-electrode system, employing graphite rod, Ag/AgCl, 1 M $MgCl_2$ as the counter electrode, reference electrode, and electrolyte, respectively. As displayed in Figure 2A, the cyclic voltammetry (CV) curves of D-CuHCF@CNTF and D-K_2CuHCF@CNTF show three pairs of redox peaks, corresponding to the redox of Fe^{3+}/Fe^{2+} and Cu^{2+}/Cu^{+}, respectively. Meanwhile, K_2CuHCF@CNTF achieves a weak current signal due to the activity limitation, resulting in inconspicuous redox peaks. Compared with these of D-K_2CuHCF@CNTF and K_2CuHCF@CNTF, the CV curve of D-CuHCF@CNTF possesses much higher current density, indicating its improved Mg-storage capability. Meanwhile, a series of precursors (CNTF, Cu@CNTF, and CuO@CNTF) during the growth process show a near-zero capacity contribution (Figure S10). A typical galvanostatic charge–discharge (GCD) curve of D-CuHCF@CNTF at 0.5 A g^{-1} also reveals three discharge platforms (Figure 2B), which is consistent with the CV result. Moreover, the D-CuHCF@CNTF delivers a much higher discharge capacity (146.6 mAh g^{-1}) than D-K_2CuHCF@CNTF (41.5 mAh g^{-1}) and K_2CuHCF@CNTF (16.1 mAh g^{-1}). The excellent Mg^{2+} storage property of D-CuHCF@CNTF mainly originated from abundant K-vacancy cavities and Cu defects, supplying convenient channels for Mg^{2+} insertion/extraction. Thus, it could avoid the Jahn–Teller distortions, and improve ion migration rate and electrode reaction reversibility. In addition, a portion of crystal water contained in D-CuHCF@CNTF forms a hydration shell to reduce the electrostatic repulsion between Mg^{2+} and D-CuHCF@CNTF. Moreover, the rate performances of D-CuHCF@CNTF, D-K_2CuHCF@CNTF, and K_2CuHCF@CNTF originating from the GCD curves (Figure S11) are compared in Figure 2C. The D-CuHCF@CNTF manifests discharge capacity of 146.6, 135.9, 124.6, 109.7, and 96.1 mAh g^{-1} when measured at the current density of 0.5, 1.0, 2.0, 5.0, and 10.0 A g^{-1}. To gain a deeper understanding of the Mg^{2+} storage behavior of D-CuHCF@CNTF, the first 20 cycles CV was measured in Figure 2D. The cathodic peak of the first cycle began at ~0.4 V, implying a certain amount of Cu^{2+} in D-CuHCF@CNTF. Then, the two anodic peaks at around 0.28 and 0.87 V correspond to the Cu^{2+} and Fe^{3+}, respectively. Furthermore, three pairs of redox peaks appeared, and the peaks were stable after multiple cycles due to the electrochemical stability of Mg^{2+} insertion/extraction. As depicted in Figure 2E, CV measurements at various scan rates were tested to reveal the electrochemical kinetics. The equation can be defined to describe the capacity contributions of the capacitive and diffusion control process: $i = aV^b$, where the a and b are regulable. By fitting the plots of log(i) versus log(V), the b value of oxide peaks (O_1, O_2, and O_3) and reduction peaks (R_1, R_2, and R_3) are 0.99, 0.78, 0.79, 0.98, 0.73, and 0.95, demonstrating that the electrochemical behavior is controlled by capacitive (Figure S12A), and the capacitive contribution attained 77.2% at 5 mV s^{-1} (Figures 2F and S12B). In comparison, the lower capacitive contributions of D-K_2CuHCF@CNTF (Figures S13 and S14) and K_2CuHCF@CNTF (Figures S15 and S16) indicate the relatively slow kinetics. Besides, the stability testing at 10 A g^{-1} demonstrates the favorable durability of D-CuHCF@CNTF (Figure 2G). As shown in Figure 2H, the relevant electrochemical indicators, including capacity retention, reversible capacity, discharge plateau and more, are far superior to other previously reported CuHCF materials, which further demonstrates the superiority of the structure of D-CuHCF@CNTF with dual-active sites.

2.3 | Mechanism characterization of D-CuHCF@CNTF

To investigate the energy-storage mechanism of the high-capacity D-CuHCF@CNTF cathode, ex situ XPS measurements were carried out at its diverse discharge/charge states (Figure 3A). As shown in Figure 3B, the ratio of Fe^{3+}/Fe^{2+} preferentially decreased following the Mg^{2+} insertion from a to c process, indicating the prior electrochemical activity of Fe^{3+}/Fe^{2+} pair. Then, the remaining embedded Mg^{2+} react with the activated Cu^{2+} until all the active sites are fully reacted (Figure 3C). After the subsequent charging process, the active sites with reduced low-valence states start to revert to the high-valence states along with Mg^{2+} extraction, which is unusual with most Cu-PBAs. Therefore, the generated high capacity could be attributed to dual-active sites that two redox-active couples (Fe^{3+}/Fe^{2+} and Cu^{2+}/Cu^{+}) participate in electron transfer reactions. As comparison, the ex situ XPS spectra were also applied to D-K_2CuHCF@CNTF and K_2CuHCF@CNTF, as presented in Figures S17 and S18. For D-K_2CuHCF@CNTF, the variation of the Cu^{2+}/Cu^{+} ratio during the discharge/charge process demonstrates that a portion of the Cu involved in electron transfer and

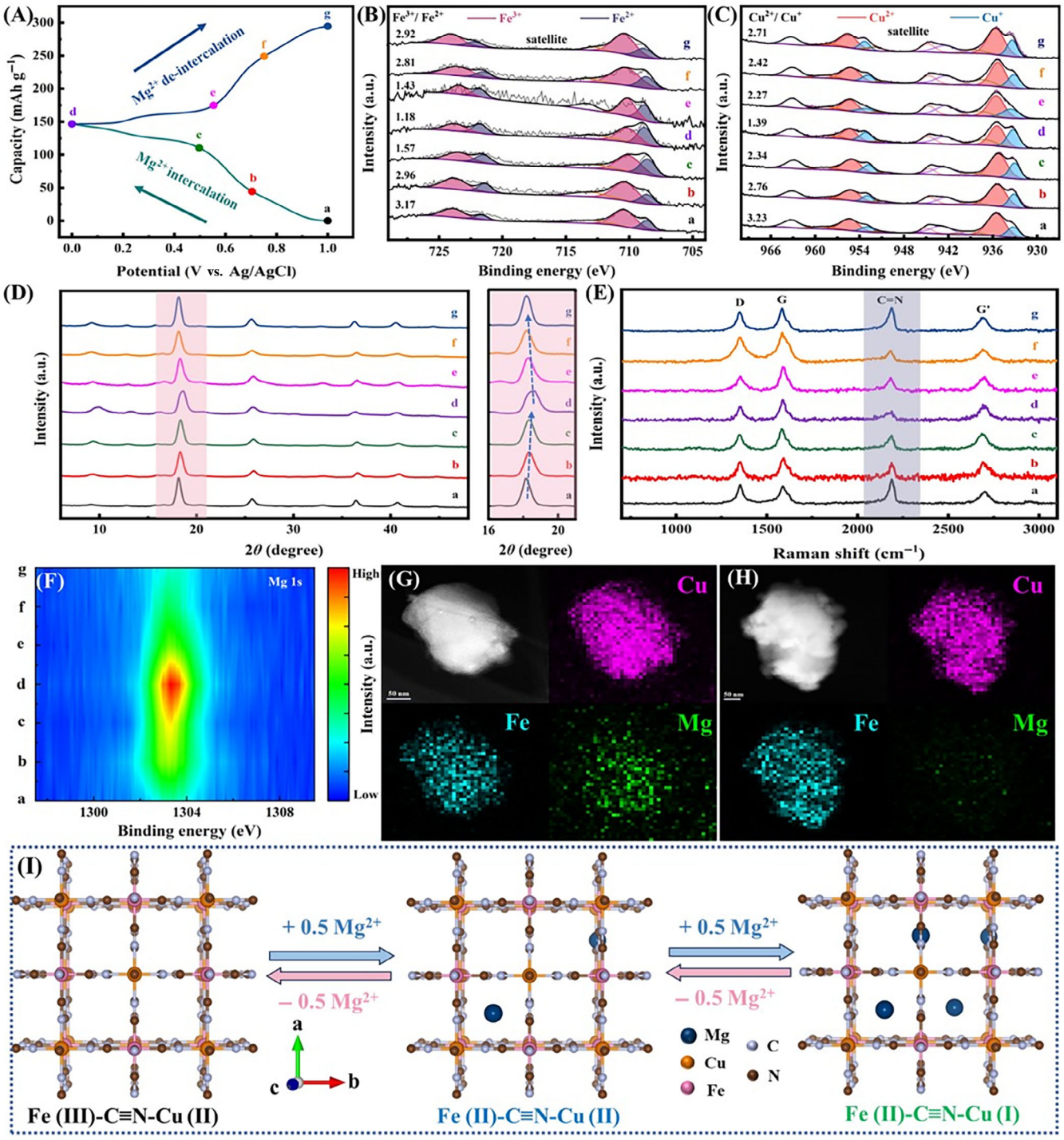

FIGURE 3 Mechanism characterization of D-CuHCF@CNTF. (A) The charge/discharge curves of the D-CuHCF@CNTF at 0.5 A g^{-1}. Ex situ XPS spectra of (B) Fe 2p and (C) Cu 2p in D-CuHCF@CNTF with varietal charge/discharge states. (D) Ex situ SAXS patterns and (E) Raman spectra of D-CuHCF@CNTF at diverse charge/discharge states. Ex situ XPS spectra of (F) Mg 1s in D-CuHCF@CNTF at different charge/discharge states. TEM images and corresponding EDX elemental mapping of the D-CuHCF at (G) a fully discharged state and (H) a subsequently fully charged state. (I) Schematic diagram of Mg^{2+} insertion/extraction process in D-CuHCF.

contributed capacity to a certain extent (Figure S17A). However, the Cu^{2+}/Cu^{+} ratio in K_2CuHCF@CNTF shows zero changes from a to e state (Figure S18B), which is in line with single-electron pair (Fe^{3+}/Fe^{2+}) of most CuHCF reported previously. Based on the above analysis, the presence of defects facilitates the activation of Cu active site. To verify the effect of Mg-storage behavior on the crystal structure, ex situ SAXS of

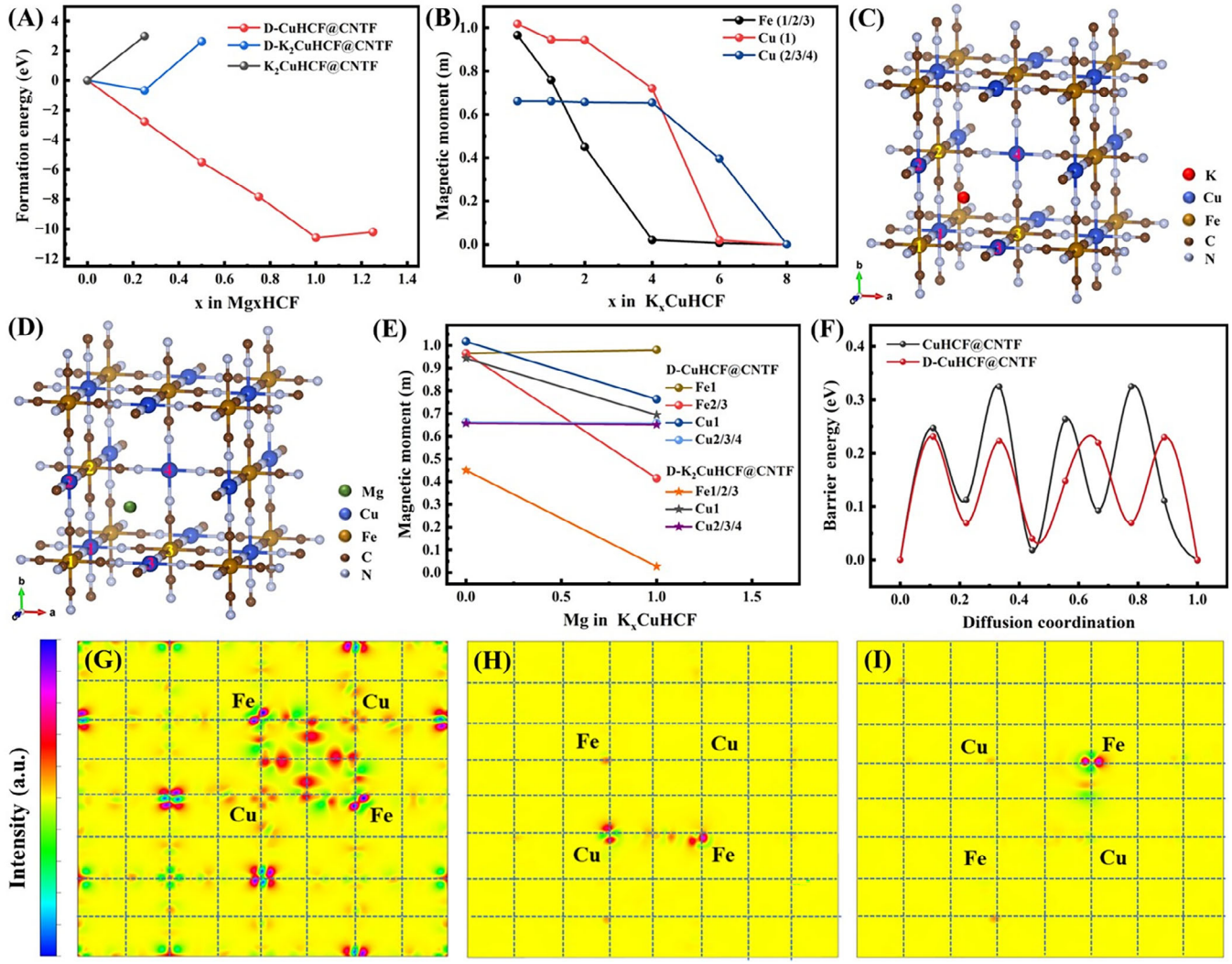

FIGURE 4 Theoretical calculation simulation. (A) Calculated formation energy of Mg intercalation in to D-CuHCF, D-K_2CuHC, and K_2CuHCF. (B) Magnetic moment of Fe and Cu and (C) corresponding structure of K intercalation in to CuHCF. (D) Structure of Mg intercalation in to D-CuHCF and (E) corresponding magnetic moment of Fe and Cu. (F) Calculated Mg diffusion barrier in CuHCF and D-CuHCF. Charge density difference section along the (001) plane of (G) D-CuHCF, (H) D-K_2CuHCF, and (I) K_2CuHCF. The red and blue represent the electron depletion and accumulation, respectively.

D-CuHCF@CNTF was carried out. No new peaks emerged during the discharge/charge process (a to g), indicating a single-phase solid solution reaction without the change of crystal framework with the insertion and deintercalation of Mg^{2+} (Figure 3D). In detail, the diffraction peaks of D-CuHCF@CNTF shift to the larger diffraction angles during the discharging process, implying the d-spacing decreases gradually accompanied by the insertion of Mg^{2+}. Then, the characteristic peaks recover to the pristine states after the subsequent charging process, indicating its excellent reversibility of Mg-storage behavior. Compared with other intercalation compounds, the contrary change in d-spacing is attributed to the shorter length of Fe^{II}-C bond compared with Fe^{III}-C in PBAs. Another powerful representation originates from Raman spectra of D-CuHCF@CNTF at the various discharge/charge states (Figure 3E), in which the relative intensity of C≡N vibration modes at about 2171 cm^{-1} varies from weak to strong along with the Mg^{2+} insertion/extraction.[59] In the XPS spectra for Mg 1s (Figure 3F), the intensity of Mg signal gradually strengthens/weakens along with the discharge/charge processes. Besides, TEM images and corresponding EDX elemental mapping images of D-CuHCF@CNTF at full-discharge and full-charge states are illustrated in Figure 3G,H, in which the appearance and disappearance of Mg further suggests the Mg^{2+} insertion/extraction mechanism during the charging/discharging process. To exhibit graphically the process of Mg-storage mechanism in D-CuHCF@CNTF, we performed a model simulation

in Figure 3I. Due to the existence of the K-vacancy cavities, more active sites and transport channels provide a larger space to store and release Mg^{2+} in D-CuHCF@CNTF. Different from the K^+, the Mg^{2+} is embedded in the face centers of the cubic phases, and a cell unit of D-CuHCF@CNTF can accommodate 1 Mg^{2+} to minimize the overall structural energy. According to the schematic diagram, the process of Mg^{2+} intercalation could be described as the pair of Fe^{3+}/Fe^{2+} first participated in the electron transfer, followed by the Cu^{2+}/Cu^{+}, which demonstrates the dual-active sites (Fe^{3+}/Fe^{2+} and Cu^{2+}/Cu^{+}) of D-CuHCF@CNTF and reveals the pivotal factor for the capacity improvement.

2.4 | Theoretical calculation simulation

Density functional theory (DFT) calculations were performed to investigate the mechanisms of Mg-ion storage in D-CuHCF, D-K_2CuHCF, and K_2CuHCF. The theoretical capacity of the three samples was studied and illustrated in Figure 4A. Due to the existence of K, the Mg-storage capacities of D-K_2CuHCF and K_2CuHCF are quite low. For the K_2CuHCF, no Mg can be stored and the defects in D-K_2CuHCF allow the sample to store 0.2 Mg (the knee point of the line) at maximum. However, when the K atoms are completely removed from K_2CuHCF, a model presenting sample A and the Mg-storage capacity can thus be pronouncedly increased to 1. To reveal the electrochemistry activities of the transition metals of Cu and Fe, their magnetic moment variations as a function of the interaction amount of K are plotted in Figure 4B,C shows the intercalation site of the 1st K in D-CuHCF. Due to the existence of the defect, the Cu atoms can be divided into two kinds, Cu (1) coordinating with 6 N atoms and Cu (2/3/4) coordinating with 4 N atoms. At the very beginning of the K intercalation, only the magnetic moment of Fe varies a lot, while both Cu (1) and Cu (2/3/4) keep their magnetic moments almost unchanged. With the increasing amount of the intercalated K, the magnetic moments of Cu (1) and Cu (2/3/4) decrease. The results suggest that both the Fe and Cu atoms exhibit their electrochemistry activities during the storage process of Mg ions into CuHCF, and Fe atom has higher activity than Cu atom. The similar conclusions can be obtained for the storage of Mg in CuHCF, as the structure (Figure 4D) and magnetic moment variations (Figure 4E) show. Since the Mg^{2+} insertion point is located at the center of the plane, composed of Cu (1/2) and Fe (2/3), according to the insertion results, only Fe (2/3) and Cu (1) in the same plane possess reaction activity in D-CuHCF. There is a little discrepancy in D-K_2CuHCF, in which the Fe (1/2/3) all express activity due to the existence of K. In general, the dual-active sites in D-CuHCF and K_2CuHCF depend on the difference of K and the degree of Cu defects. Meanwhile, the existence of Cu defects is found to be conducive to the diffusion of Mg in CuHCF, as shown in Figure 4F, where the results indicate that the diffusion barrier of Mg in pristine CuHCF of ~3.3 eV decreases to ~2.3 eV in the defective CuHCF. Based on the experimental observations, small amount of K in D-K_2CuHCF and K_2CuHCF could be de-intercalated and make Mg intercalate into the CuHCF during the charge–discharge cycles. To analyze the active sites, the charge density difference pictures are shown in Figure 4G–I. For the D-CuHCF, the charge differences for both Fe and Cu are apparent, indicating that they are electrochemical active in Figure 4G. The D-K_2CuHCF sample in Figure 4H also confirms that both Fe and Cu are active although the charge variation are smaller than the D-CuHCF. For the D-K_2CuHCF (Figure 4I), only the Fe atom could be identified as the active site since there exists no apparent charge difference around the Cu atom.

2.5 | Assembly and electrochemical characterization of flexible fiber battery devices

To assemble a "rocking-chair" type FAMIB, a suitable Mg-ion intercalation-type anode needs to be developed. $NaTi_2(PO_4)_3$ (NTP), as a polyanionic anode with a three-dimensional polyanionic skeleton, exhibits high ionic conductivity and structural stability for Li/Na-ion storage. Based on the above advantages, we choose the NTP@CNTF as an anode material to analyze its Mg-storage performance. Rugby ball-like NTP was grown on the surface of CNTF by a hydrothermal method (Figure S19). The crystal structure and chemical composition were studied by the XRD (Figure S20) and Raman (Figure S21). As displayed in the GCD curves (Figure S22), NTP@CNTF achieves a volumetric capacity of 101.5 mAh cm^{-3} at 1 A cm^{-3} and it still retains a high-capacity retention of 52.8 mAh cm^{-3} when the current density up to 10 A cm^{-3}, proving its impressive Mg-storage capacity and rate performance. Simultaneously, CV curves at various scan rates from 1 to 5 mV s^{-1} were measured, in which typical redox peaks located in ~1.28 V (peak 1) and ~1.05 V (peak 2). The corresponding b values are equal to 0.53 and 0.66, respectively, which represent the electrode reaction mainly belongs to diffusion control (Figure S23). More importantly, NTP@CNTF shows extraordinary rate performance (Figure S24) and outstanding cycle stability with negligible degradation after 1000 charge/discharge cycles at 10 A cm^{-3} (Figure S25).

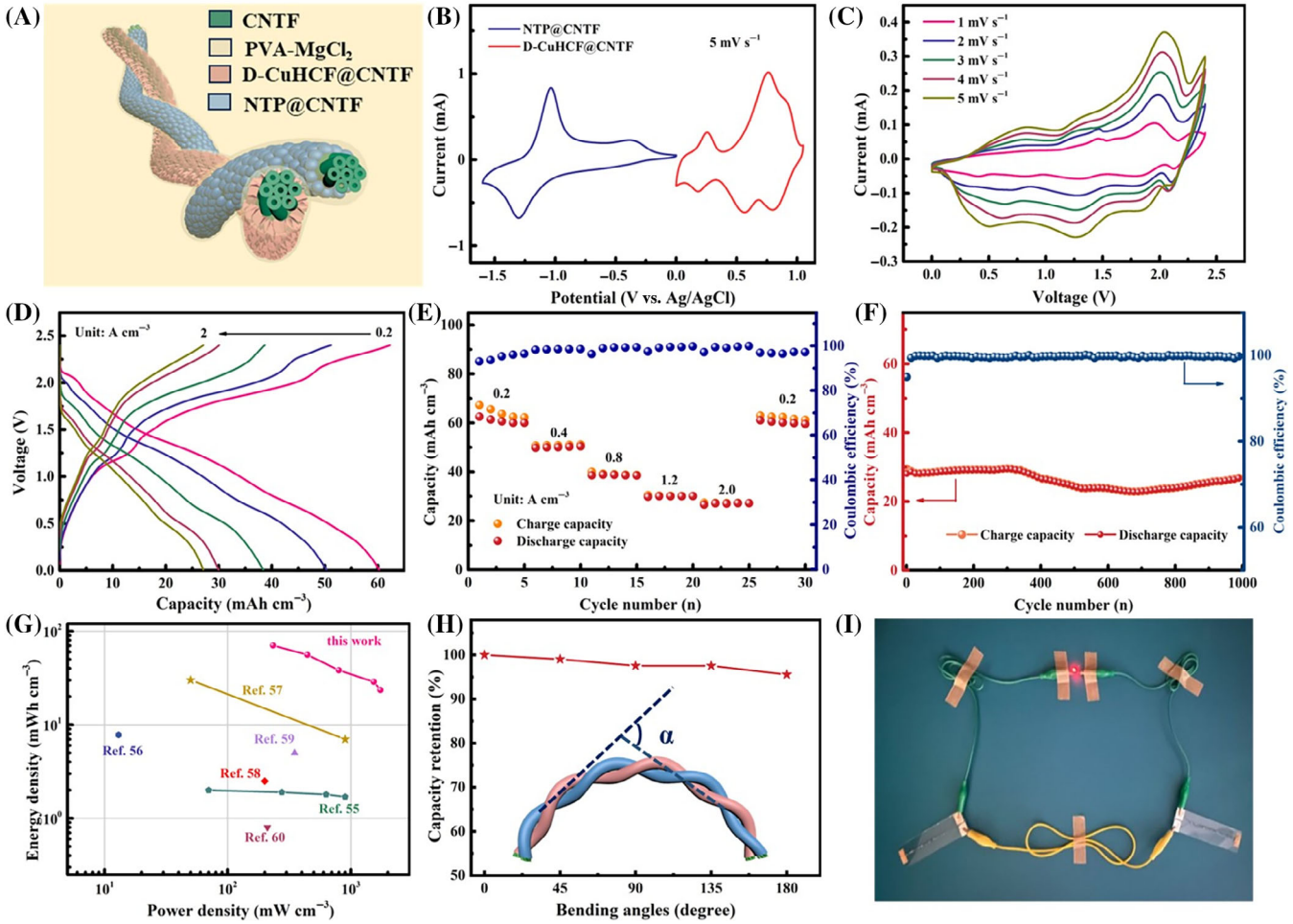

FIGURE 5 Assembly and electrochemical characterization of flexible fiber battery devices. (A) Schematic diagram of the FAMIB. (B) CV curves of D-CuHCF@CNTF and NTP@CNTF at 5 mV s^{-1}, respectively. (C) CV plots of our FAMIB at various scan rates. (D) GCD curves and (E) rate performance of FAMIB with different current density from 0.2 to 2.0 A cm^{-3}. (F) Cycling stability of FAMIB at 2.0 A cm^{-3}. (G) Ragone plots. (H) Capacity retention of FAMIB under different bending angles. (I) Photograph of a red LED powered by the two FAMIBs connected in series.

Given the excellent Mg-storage electrochemical behavior of D-CuHCF@CNTF cathode and NTP@CNTF anode, a FAMIB with twisted structure was successfully constructed by employing polyvinyl alcohol-$MgCl_2$ (PVA-$MgCl_2$) gel electrolyte, as illustrated in Figure 5A. Figure 5B displays the CV curves of D-CuHCF@CNTF cathode and NTP@CNTF anode, which is expected to build a high-voltage FAMIB. As expected, CV curves of the as-assembled FAMIB with various scan rates from 1 to 5 mV s^{-1} were measured, in which three pairs of typical redox peaks were identified (Figure 5C). As presented in Figure 5D, a high volumetric capacity of 60.2 mAh cm^{-3} at 0.2 A cm^{-3} is achieved for our FAMIB. When the current density recovers to 0.2 A cm^{-3}, a reversible capacity of 59.5 mAh cm^{-3} can still be maintained (Figure 5E). Furthermore, the FAMIB delivers superior cycling stability with 92.7% of the initial capacity after 1000 cycles (Figure 5F). More encouragingly, the FAMIB yields a remarkable energy density of 66.3 mWh cm^{-3} at a power density of 0.22 mW cm^{-3}, outperforming most recently reported fiber-based aqueous batteries reported (Figure 5G).[60–65] More notably, there is a negligible capacity change under various bending angles (Figures 5H and S26), proving the superior mechanical flexibility. Impressively, two FAMIBs connected in series can light up a red LED light (Figure 5I), which verifies the feasibility of FAMIBs acting as power sources.

3 | CONCLUSION

In conclusion, we successfully fabricated the freestanding D-CuHCF with structural water via organic acid co-coordination and etching strategy, which serves as a novel cathode for AMIBs. Specifically, Cu^{2+} co-coordinates with $K_3[Fe(CN)_6]$ and $C_9H_6O_6$ to form 3D

D-CuHCF nanosheet arrays. The newly-developed D-CuHCF@CNTF takes advantage of its dual-active sites and charge shielding effect to yield a high discharge capacity of 146.6 mAh g^{-1} (0.5 A g^{-1}). Experimental and computational results reveal the energy-storage mechanism of D-CuHCF, involving the redox reactions of Fe and Cu during the Mg^{2+} insertion/extraction process. To highlight, the D-CuHCF/CNTF cathode and $NaTi_2(PO_4)_3$/CNTF anode can be coupled to construct a rocking-chair FAMIB, achieving admirable energy density and exceptional flexibility. This work provides a feasible strategy to explore high-capacity PBA cathode materials with two-electron reaction for high-energy-density wearable AMIBs.

4 | EXPERIMENTAL SECTION

4.1 | Synthesis of D-CuHCF@CNTF

CuO nanosheets were prepared by a typical oxidization process evolved from the aforementioned Cu@CNTF. The Cu@CNTF was placed into the oxidizing solution, consisting of 10 mol L^{-1} NaOH, 1 mol L^{-1} $(NH_4)_2S_2O_8$, and a certain amount of deionized water. After oxidation reaction for 24 h, the black sample was washed with deionized water and ethanol, then dried in air at room temperature (named CuO@CNTF). The above-mentioned CuO@CNTF was immersed in deionized water and ethanol mixed solution with 0.015 M 1,3,5-benzenetricarboxylic acid (H_3BTC) and 0.05 M of $K_3Fe(CN)_6$ for 24 h. Finally, the product was washed with deionized water and ethanol, and dried in air at room temperature (named D-CuHCF@CNTF).

4.2 | Synthesis of NTP@CNTF

Exactly 1 mL $TiCl_3$ (30 wt% HCl) was added into 30 mL ethylene glycol and stirred for 30 min, then 1 mL H_3PO_4 was dropped into the above solution. After stirring for 30 min, 1.0 g $NaH_2PO_4 \cdot 2H_2O$ was placed into the above solution under continuous stirring. After dissolution, the resulting mixed solution was transferred to a Teflon-lined stainless-steel autoclave with CNTF current collectors. The solvothermal reaction was kept at 150°C for 6 h, then the obtained sample was rinsed with ethanol, dried in air and named NTP@CNTF.

4.3 | Assembling of the FAMIB

First, 9.5 g $MgCl_2$ and 10 g PVA were dissolved in 100 mL deionized water and heated at 95°C under stirring for 2 h to form a homogeneous PVA/$MgCl_2$ gel electrolyte. Subsequently, the D-CuHCF@CNTF cathode and NTP@CNTF anode were dipped in PVA/$MgCl_2$ gel electrolyte and dried at 60°C for 10 min. Finally, the FAMIBs device was fabricated by twisting the D-CuHCF@CNTF cathode and NTP@CNTF anode coated with the PVA/$MgCl_2$ gel electrolyte.

ACKNOWLEDGMENTS

This work was supported by the National Key R&D Program of China (2022YFA1203304), the Natural Science Foundation of Jiangsu Province (BK20220288), Suzhou Institute of Nano-Tech and Nano-Bionics, Chinese Academy of Sciences (Start-up grant E1552102). We are grateful for the synthesis analysis from Dr. Yahan Shan and the technical support of 2D GIWAXS for Nano-X from Suzhou Institute of Nano-Tech and Nano-Bionics, Chinese Academy of Sciences.

CONFLICT OF INTEREST STATEMENT

The authors declare no conflict of interest.

ORCID

Qichong Zhang https://orcid.org/0000-0003-1627-3946

REFERENCES

1. Guan C, Liu X, Ren W, Li X, Cheng C, Wang J. Rational design of metal-organic framework derived hollow $NiCo_2O_4$ arrays for flexible supercapacitor and electrocatalysis. *Adv Energy Mater*. 2017;7(12):1602391.
2. Yan Y, Liu X, Yan J, Guan C, Wang J. Electrospun nanofibers for new generation flexible energy storage. *Energy Environ Mater*. 2021;4(4):502-521.
3. Li X, Chen L, Yuan S, et al. Stretchable luminescent perovskite-polymer hydrogels for visual-digital wearable strain sensor textiles. *Adv Fiber Mater*. 2023;5(5):1671-1684.
4. Wang M, Wang Q, Ding X, et al. The prospect and challenges of sodium-ion batteries for low-temperature conditions. *Interdiscip Mater*. 2022;1(3):373-395.
5. Luo Q, Ming L, Zhang D, et al. Constructing Br-doped $Li_{10}SnP_2S_{12}$-based all-solid-state batteries with superior performances. *Energy Mater Adv*. 2023;4:0065.
6. Rashad M, Asif M, Wang Y, He Z, Ahmed I. Recent advances in electrolytes and cathode materials for magnesium and hybrid-ion batteries. *Energy Storage Mater*. 2020;25(3):342-375.
7. Yang Z, Liu X-H, He X-X, et al. Rechargeable sodium-based hybrid metal-ion batteries toward advanced energy storage. *Adv Funct Mater*. 2021;31(8):2006457.
8. Hou Z, Zhang T, Liu X, et al. A solid-to-solid metallic conversion electrochemistry toward 91% zinc utilization for sustainable aqueous batteries. *Sci Adv*. 2022;8(41):eabp8960.
9. Wu N, Yang Y-J, Zhang Q-Y, Zhang X, du XN. A layered titanium-based transition metal oxide as stable anode material for magnesium-ion batteries. *J Mater Sci*. 2020;55(35):16674-16682.
10. Koketsu T, Ma J, Morgan BJ, et al. Reversible magnesium and aluminium ions insertion in cation-deficient anatase TiO_2. *Nat Mater*. 2017;16(11):1142-1148.

11. Su H, Jaffer S, Yu H. Transition metal oxides for sodium-ion batteries. *Energy Storage Mater*. 2016;5(10):116-131.
12. Xu Y, Deng X, Li Q, et al. Vanadium oxide pillared by interlayer Mg^{2+} ions and water as ultralong-life cathodes for magnesium-ion batteries. *Chem*. 2019;5(5):1194-1209.
13. Zhu Y-F, Xiao Y, Dou S-X, Kang YM, Chou SL. Spinel/post-spinel engineering on layered oxide cathodes for sodium-ion batteries. *eScience*. 2021;1(1):13-27.
14. Truong QD, Devaraju MK, Honma I. Nanocrystalline $MgMnSiO_4$ and $MgCoSiO_4$ particles for rechargeable Mg-ion batteries. *J Power Sources*. 2017;361(9):195-202.
15. Feng Z, Yang J, NuLi Y, Wang J. Sol–gel synthesis of $Mg_{1.03}Mn_{0.97}SiO_4$ and its electrochemical intercalation behavior. *J Power Sources*. 2008;184(2):604-609.
16. Chen L, Bao J, Dong X, et al. Aqueous Mg-ion battery based on polyimide anode and Prussian blue cathode. *ACS Energy Lett*. 2017;2(5):1115-1121.
17. Komayko AI, Ryazantsev SV, Trussov IA, et al. The misconception of Mg^{2+} insertion into Prussian blue analogue structures from aqueous solution. *ChemSusChem*. 2021;14(6):1574-1585.
18. Yang Y, Zhou J, Wang L, et al. Prussian blue and its analogues as cathode materials for Na-, K-, Mg-, Ca-, Zn- and Al-ion batteries. *Nano Energy*. 2022;99:107424.
19. Sun X, Duffort V, Nazar LF. Prussian blue Mg-Li hybrid batteries. *Adv Sci*. 2016;3(8):1600044.
20. Dong X, Chen L, Su X, Wang Y, Xia Y. Flexible aqueous lithium-ion battery with high safety and large volumetric energy density. *Angew Chem Int Ed*. 2016;55(26):7474-7477.
21. Liu Q, Hu Z, Chen M, et al. The cathode choice for commercialization of sodium-ion batteries: layered transition metal oxides versus Prussian blue analogs. *Adv Funct Mater*. 2020;30(14):1909530.
22. Hu Y, Guan C, Feng G, Ke Q, Huang X, Wang J. Flexible asymmetric supercapacitor based on structure-optimized Mn_3O_4/reduced graphene oxide nanohybrid paper with high energy and power density. *Adv Funct Mater*. 2015;25(47):7291-7299.
23. Wang Q, Li J, Jin H, Xin S, Gao H. Prussian-blue materials: revealing new opportunities for rechargeable batteries. *InfoMat*. 2022;4(6):e12311.
24. Ma L, Cui H, Chen S, Li X, Dong B, Zhi C. Accommodating diverse ions in Prussian blue analogs frameworks for rechargeable batteries: the electrochemical redox reactions. *Nano Energy*. 2021;81:105632.
25. Zheng R, Li Y, Yu H, et al. Ammonium ion batteries: material, electrochemistry and strategy. *Angew Chem Int Ed*. 2023;62(23):e202301629.
26. Xu C, Yang Z, Zhang X, et al. Prussian blue analogues in aqueous batteries and desalination batteries. *Nano-Micro Lett*. 2021;13(1):166.
27. He H, Huang D, Tang Y, et al. Tuning nitrogen species in three-dimensional porous carbon via phosphorus doping for ultra-fast potassium storage. *Nano Energy*. 2019;57(3):728-736.
28. Wang K, Fan X, Chen S, et al. 3D Co-doping α-$Ni(OH)_2$ nanosheets for ultrastable, high-rate Ni-Zn battery. *Small*. 2022;19(8):e2206287.
29. Zhang Y, Li J, Zhao W, et al. Defect-free metal–organic framework membrane for precise ion/solvent separation toward highly stable magnesium metal anode. *Adv Mater*. 2022;34(6):2108114.
30. Shimokawa K, Atsumi T, Okamoto NL, et al. Structure design of long-life spinel-oxide cathode materials for magnesium rechargeable batteries. *Adv Mater*. 2021;33(7):2007539.
31. Bae J, Park H, Guo X, Zhang X, Warner JH, Yu G. High-performance magnesium metal batteries via switching the passivation film into a solid electrolyte interphase. *Energ Environ Sci*. 2021;14(8):4391-4399.
32. Liu F, Wang T, Liu X, Fan LZ. Challenges and recent progress on key materials for rechargeable magnesium batteries. *Adv Energy Mater*. 2021;11(2):2000787.
33. Zhu F, Zhang H, Lu Z, Kang D, Han L. Controlled defective engineering of MoS_2 nanosheets for rechargeable Mg batteries. *J Energy Storage*. 2021;42:103046.
34. Liang G, Mo F, Li H, et al. A universal principle to design reversible aqueous batteries based on deposition-dissolution mechanism. *Adv Energy Mater*. 2019;9(32):1901838.
35. Ma L, Chen S, Long C, et al. Achieving high-voltage and high-capacity aqueous rechargeable zinc ion battery by incorporating two-species redox reaction. *Adv Energy Mater*. 2019;9(45):1902446.
36. Fu Q, Wu X, Luo X, et al. High-voltage aqueous Mg-ion batteries enabled by solvation structure reorganization. *Adv Funct Mater*. 2022;32(16):2110674.
37. Shen Y, Zhang Q, Wang Y, Gu L, Zhao X, Shen X. A pyrite iron disulfide cathode with a copper current collector for high-energy reversible magnesium-ion storage. *Adv Mater*. 2021;33(41):2103881.
38. Tang Y, Li X, Lv H, et al. High-energy aqueous magnesium hybrid full batteries enabled by carrier-hosting potential compensation. *Angew Chem Int Ed*. 2021;60(10):5443-5452.
39. Leong KW, Pan W, Wang Y, Luo S, Zhao X, Leung DYC. Reversibility of a high-voltage, Cl^--regulated, aqueous Mg metal battery enabled by a water-in-salt electrolyte. *ACS Energy Lett*. 2022;7(8):2657-2666.
40. Du A, Zhang H, Zhang Z, et al. A crosslinked polytetrahydrofuran-borate-based polymer electrolyte enabling wide-working-temperature-range rechargeable magnesium batteries. *Adv Mater*. 2019;31(11):1805930.
41. Xu Y, Liu Z, Zheng X, et al. Solid electrolyte Interface regulated by solvent-in-water electrolyte enables high-voltage and stable aqueous Mg-MnO_2 batteries. *Adv Energy Mater*. 2022;12(22):2103352.
42. Mizuno Y, Okubo M, Hosono E, et al. Electrochemical Mg^{2+} intercalation into a bimetallic CuFe Prussian blue analog in aqueous electrolytes. *J Mater Chem A*. 2013;1(42):13055-13059.
43. Liu Y, He G, Jiang H, Parkin IP, Shearing PR, Brett DJL. Cathode design for aqueous rechargeable multivalent ion batteries: challenges and opportunities. *Adv Funct Mater*. 2021;31(13):2010445.
44. Zeng Y, Lu XF, Zhang SL, Luan D, Li S, Lou XW(D). Construction of Co-Mn Prussian blue analog hollow spheres for efficient aqueous Zn-ion batteries. *Angew Chem Int Ed*. 2021;60(41):22189-22194.
45. Li H, Okamoto NL, Hatakeyama T, Kumagai Y, Oba F, Ichitsubo T. Fast diffusion of multivalent ions facilitated by concerted interactions in dual-ion battery systems. *Adv Energy Mater*. 2018;8(27):1801475.

46. Sun D, Zhu X, Luo B, et al. New binder-free metal phosphide-carbon felt composite anodes for sodium-ion battery. *Adv Energy Mater*. 2018;8(26):1801197.
47. Xie B, Zuo P, Wang L, et al. Achieving long-life Prussian blue analogue cathode for Na-ion batteries via triple-cation lattice substitution and coordinated water capture. *Nano Energy*. 2019;61(7):201-210.
48. Zhang X, Xia M, Yu H, et al. Hydrogen bond-assisted ultra-stable and fast aqueous NH_4^+ storage. *Nano-Micro Lett*. 2021;13(1):139.
49. Li J, Luo N, Kang L, et al. Hydrogen-bond reinforced super-structural manganese oxide as the cathode for ultra-stable aqueous zinc ion batteries. *Adv Energy Mater*. 2022;12(44):2201840.
50. Zeng Y, Xu J, Wang Y, Li S, Luan D, Lou XW(D). Formation of CuMn Prussian blue analog double-shelled nanoboxes toward long-life Zn-ion batteries. *Angew Chem Int ed*. 2022;61(48):e202212031.
51. Wang RY, Shyam B, Stone KH, et al. Reversible multivalent (monovalent, divalent, trivalent) ion insertion in open framework materials. *Adv Energy Mater*. 2015;5(12):1401869.
52. Gao X, Wu H, Su C, et al. Recent advances in carbon-based nanomaterials for multivalent-ion hybrid capacitors: a review. *Energy Environ Sci*. 2023;16(4):1364-1383.
53. Liu L, Niu Z, Chen J. Unconventional supercapacitors from nanocarbon-based electrode materials to device configurations. *Chem Soc Rev*. 2016;45(15):4340-4363.
54. Nam KW, Kim S, Lee S, et al. The high performance of crystal water containing manganese birnessite cathodes for magnesium batteries. *Nano Lett*. 2015;15(6):4071-4079.
55. Wang L, Zhu Y, Wen Y, et al. Regulating the local charge distribution of Ni active sites for the urea oxidation reaction. *Angew Chem Int ed*. 2021;60(19):10577-10582.
56. Zhang Q, Man P, He B, et al. Binder-free $NaTi_2(PO_4)_3$ anodes for high-performance coaxial-fiber aqueous rechargeable sodium-ion batteries. *Nano Energy*. 2020;67:104212.
57. Shi X, Zuo Y, Zhai P, et al. Large-area display textiles integrated with functional systems. *Nature*. 2021;591(7849):240-245.
58. Sun H, You X, Deng J, et al. Novel graphene/carbon nanotube composite fibers for efficient wire-shaped miniature energy devices. *Adv Mater*. 2014;26(18):2868-2873.
59. Shen Y, Zou J, Lan H, et al. Unlocking Prussian blue analogues inert-site to achieve high-capacity ammonium storage. *Adv Funct Mater*. 2024;2400598.
60. Li Z, Shao M, Zhou L, et al. A flexible all-solid-state micro-supercapacitor based on hierarchical CuO@layered double hydroxide core–shell nanoarrays. *Nano Energy*. 2016;20(2):294-304.
61. Yu D, Goh K, Wang H, et al. Scalable synthesis of hierarchically structured carbon nanotube-graphene fibres for capacitive energy storage. *Nat Nanotechnol*. 2014;9(7):555-562.
62. Guo Z, Zhao Y, Ding Y, et al. Multi-functional flexible aqueous sodium-ion batteries with high safety. *Chem*. 2017;3(2):348-362.
63. Huang Y, Ip WS, Lau YY, et al. Weavable, conductive yarn-based NiCo//Zn textile battery with high energy density and rate capability. *ACS Nano*. 2017;11(9):8953-8961.
64. Li M, Meng J, Li Q, et al. Finely crafted 3D electrodes for dendrite-free and high-performance flexible fiber-shaped Zn-Co batteries. *Adv Funct Mater*. 2018;28(32):1802016.
65. Zeng Y, Meng Y, Lai Z, et al. An ultrastable and high-performance flexible fiber-shaped Ni–Zn battery based on a Ni–NiO heterostructured nanosheet cathode. *Adv Mater*. 2017;29(44):1702698.

SUPPORTING INFORMATION

Additional supporting information can be found online in the Supporting Information section at the end of this article.

How to cite this article: Ling Y, He B, Han L, Gong W, Chang C, Zhang Q. Two-electron redox chemistry enables potassium-free copper hexacyanoferrate as high-capacity cathode for aqueous Mg-ion battery. *InfoMat*. 2024;6(6):e12549. doi:10.1002/inf2.12549